Real-space observation of ultra-confined in-plane anisotropic acoustic THz plasmon polaritons

S. Chen[1,2*], P. L. Leng[3*], A. Konečná[4,5], E. Modin[2], M. Gutierrez[6,7], E. Vicentini[2], B. Martín-García[2], M. Barra-Burillo[2], I. Niehues[2], C. Maciel Escudero[2,6], X. Y. Xie[3], L. E. Hueso[2,8], E. Artacho[2,8,9,10], J. Aizpurua[6], I. Errea[6,10,11], M. G. Vergniory[6,12], A. Chuvilin[2,8], F. X. Xiu[3], R. Hillenbrand[2,8]

[1] Terahertz Technology Innovation Research Institute, National Basic Science Center - Terahertz Science and Technology Frontier, Terahertz Precision Biomedical Discipline 111 Project, Shanghai Key Lab of Modern Optical System, University of Shanghai for Science and Technology, Shanghai 200093, China

[2] CIC nanoGUNE BRTA, 20018 Donostia-San Sebastián, Spain

[3] State Key Laboratory of Surface Physics and Department of Physics, Institute for Nanoelectronic Devices and Quantum Computing, Zhangjiang Fudan International Innovation Center, Fudan University, Shanghai 200433, China

[4] Central European Institute of Technology, Brno University of Technology, 61200 Brno, Czech Republic

[5] Institute of Physical Engineering, Brno University of Technology, Brno 616 69, Czech Republic

[6] Materials Physics Center, CSIC-UPV/EHU, 20018 Donostia-San Sebastián, Spain

[7] Departamento de Física, Facultad de Ciencia y Tecnología, Universidad del País Vasco (UPV/EHU), 48080 Bilbao, Spain

[8] IKERBASQUE, Basque Foundation for Science, 48009 Bilbao, Spain

[9] Theory of Condensed Matter, Cavendish Laboratory, University of Cambridge, Cambridge CB3 0HE, UK

[10] Donostia International Physics Centre (DIPC), 20018 San Sebastian, Spain

[11] Departamento de Física Aplicada, Escuela de Ingeniería de Gipuzkoa, Universidad del País Vasco (UPV/EHU), 20018 Donostia/San Sebastián, Spain

[12] Max Planck for Chemical Physics of Solids, 01187 Dresden, Germany

[*] equal contribution

E-mail: r.hillenbrand@nanogune.eu, faxian@fudan.edu.cn

Thin layers of in-plane anisotropic materials can support ultra-confined polaritons, whose wavelengths depend on the propagation direction. They bear potential for exploring fundamental material properties and to develop novel nanophotonic devices. However, the real-space observation of in-plane anisotropic plasmon polaritons (PPs) - which exist in much broader spectral ranges than the recently observed in-plane anisotropic phonon polaritons - has been elusive so far.

Here, we apply THz nanoscopy to image in-plane anisotropic low-energy PPs in monoclinic Ag_2Te platelets. Hybridization of the PPs with their mirror image – by placing the platelets above a Au layer – increases the direction-dependent relative polariton propagation length, additionally to increasing the directional polariton confinement (reaching $\lambda_p/\lambda_0 \sim 1/65$, where λ_0 is the free-space photon wavelength). This allows for verifying a linear dispersion and elliptical isofrequency contour in momentum space, revealing in-plane anisotropic acoustic THz PPs. Our work shows high-symmetry (elliptical) polaritons on low-symmetry (monoclinic) crystals and also demonstrates the use of THz PPs for local measurements of anisotropic charge carrier masses and damping.

Polaritons are electromagnetic waves formed by strong coupling between light and dipolar matter excitations such as plasmons, phonons or excitons[1]. They attract wide attention due to their ability to confine and guide light at the nanometer scale, promising the development of ultra-small resonators and waveguides for sensing, heat transfer and optical circuitry applications[2-8]. The control and manipulation of polaritons can be largely expanded with naturally anisotropic materials, as the strong light confinement can be accompanied by negative phase velocities, highly directional propagation, or exotic wavefront shapes[3,7-19].

When a polaritonic material exhibits optical anisotropy along its surface, polaritons can propagate with ultrashort and direction-dependent wavelengths, promising unprecedented pathways for nanoscale guiding and manipulation of electromagnetic energy. Recently, in-plane anisotropic phonon polaritons (PhPs) were observed in natural polar materials such as α-MoO_3[12-14], α-V_2O_5[16], $CaCO_3$[17] and β-GaO[7]. They exhibit ultra-long lifetimes of up to several picoseconds, yielding long polariton propagation length despite their strongly compressed wavelength as compared to the corresponding free-space photon wavelength. On the other hand, the existence of PhPs is limited to rather narrow spectral ranges between the transverse and longitudinal optical phonon frequencies (Reststrahlen bands)[20].

Compared to PhPs, plasmon polaritons (PPs) in semiconductors and semimetals offer the advantage of being available in much broader spectral ranges and being tunable by doping. PPs with in-plane anisotropic properties were predicted for black phosphorous[21]and borophene[22,23]and observed by far-field spectroscopy of black phosphorus carbide[24] and tungsten telluride PP resonators[25]. However, the experimental visualization of propagating in-plane anisotropic PPs – particularly over several wavelengths and at frequencies of a few THz - has been elusive so far.

Ultra-confined PPs often suffer from larger damping and short propagation length compared to PhPs, with PP lifetimes often being below 0.6 ps[26-29]. In the technologically increasingly important THz spectral range, such lifetimes correspond to about one temporal oscillation cycle of the THz field. Although such times are large enough for the development of ultra-small plasmonic THz resonators[25,30], the propagation length of ultra-confined PPs in thin layers is in the range of the polariton wavelength or less[28,29,31,32], challenging their real-space observation and potential on-chip circuitry applications.

Here, we use scattering-type scanning near-field optical microscopy (s-SNOM[26,27]) to image ultra-confined in-plane anisotropic THz PPs on monoclinic Ag_2Te (Hessite) platelets. Ag_2Te is a narrow bandgap semiconductor with electron concentrations around 10^{18} cm^{-3} at room temperature, where the effective masses of the charge carriers exhibit a strong anisotropy[33-35]. We enhance the confinement and relative propagation length of the PPs by hybridizing them with their mirror image in an adjacent metal substrate, yielding acoustic plasmon polaritons (APPs). Most important, the anisotropy of the polariton propagation is qualitatively retained and the long APP propagation lengths reveal an elliptical APP isofrequency contour in the wavevector space. By crystal structure analysis using scanning transmission electron microscopy (STEM) we can explain the highly-symmetric (elliptical) polariton propagation on the low-symmetry crystals. We finally demonstrate how the elliptical APPs can be exploited for measuring in-plane anisotropic effective carrier masses.

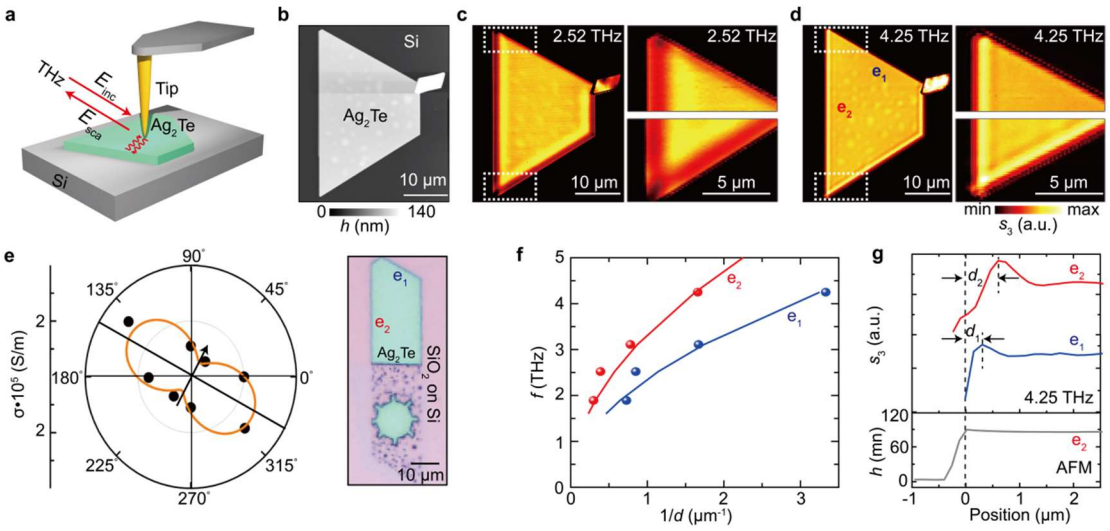

Fig. 1 | Real-space nanoimaging of in-plane anisotropic THz PPs on Ag_2Te platelets. a, Illustration of the polariton imaging experiment. E_{inc} and E_{sca} indicate the illuminating and tip-scattered field, respectively. The sine waves on the platelet indicate the tip-launched and edge-reflected PPs, respectively. **b,** Topography image of an 85 nm thick Ag_2Te platelet on Si. **c,** Left: Near-field image of the whole platelet at 2.52 THz. Right: Enlarged views of the platelet corners marked by the dashed white rectangles in the left images. **d,** Same as panel c but for 4.25 THz. **e,** Directional in-plane electrical transport measurements of a Ag_2Te platelet on SiO_2/Si substrate. Right panel: light microscopy image of a Ag_2Te platelet, whose lower part was etched to obtain a disk with small rectangular protrusions serving as contact pads. Left panel: Black dots show the directional in-plane conductivity that was measured between two diametrically opposed electrodes through the four-terminal method. Brown solid curve shows fit described in Supplementary Note 3. The black arrow marks the direction perpendicular to the edge e_1. **f,** Qualitative dispersion of PPs propagating perpendicular to the platelet edges marked e_1 and e_2 in panel d, obtained by plotting the frequency f versus $1/d_1$ (blue dots) and $1/d_2$ (red dots). d_1 and d_2 were extracted from near-field line profiles (such as the ones shown in panel g) across the platelet edges e_1 and e_2. Solid lines are guides to the eye. **g,** Near-field line profiles across the platelet edges e_1 and e_2, extracted from the near-field image at 4.25 THz (shown in panel **c**). The bottom graph shows the topography (i.e. height h) profile across the e_2 edge. The vertical dashed line marks the platelet edge. d_1 and d_2 are the distances between the platelet edge and the respective first near-field signal maximum.

Single crystalline Ag_2Te platelets were grown on sapphire by chemical vapor deposition[35] (CVD; Methods) and transferred onto different substrates. As illustrated in Fig. 1a, we performed polariton interferometry using s-SNOM (Methods and Supplementary Note S1)[26,27]. A metalized atomic force microscope (AFM) tip is illuminated with p-polarized THz radiation of frequency f, concentrating the incident field at its very apex to a nanoscale THz hot spot that excites polaritons propagating radially away from the tip. When the polaritons are reflected at the platelet edges, recording of the tip-scattered THz field as a function of tip position yields images of

polariton interference fringes with spacing of typically half the polariton wavelength, $\lambda_p/2$.

We first imaged an 85 nm-thick Ag_2Te platelet on a Si substrate, whose topography images is shown in Fig. 1b. In the THz near-field images (Fig. 1c,d) we observe a bright fringe parallel to the platelet edges, which is a typical observation for polaritons of short propagation lengths[29,36]. These fringes can be better appreciated in the THz near-field line profiles (Fig. 1g) across the edges e_1 and e_2 (Fig. 1c,d), where maxima of the near-field signal (corresponding to the fringes) can be clearly seen at distances d_1 and d_2 to the platelet edges. Plotting the frequency f versus $1/d_i$, the latter representing a qualitative proxy for the real part of the polariton wavevector, $k'_{p,i} = 2\pi/\lambda_{p,i}$[36], we observe a strong increase of $1/d_i$ with increasing f, which is a typical characteristic of a polariton dispersion (Fig. 1f). Most interestingly, the fringes parallel to the edge e_1 are much narrower and closer to the edge than the fringes parallel to the edge e_2, indicating $k'_{p,1} > k'_{p,2}$ and thus a strongly anisotropic in-plane PP dispersion.

To gain further insights, we conducted in-plane directional electric transport measurements on a Ag_2Te disk with multiple contact pads (Methods and Supplementary Note S2). We found a strongly anisotropic electrical conductivity with the lowest conductivity nearly perpendicular to the platelet edge e_1, indicating that the polariton anisotropy is related to in-plane anisotropic electronic properties.

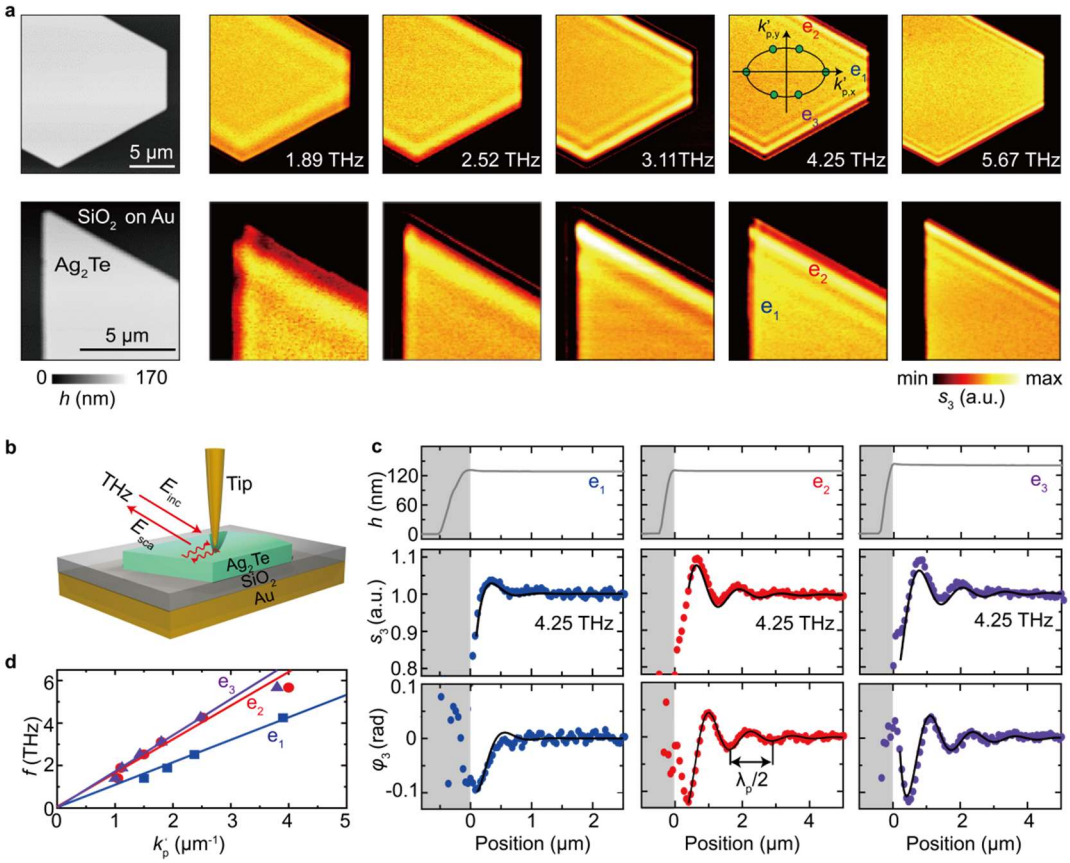

Fig. 2 | Real-space nanoimaging of in-plane anisotropic THz APPs in a $Ag_2Te/SiO_2/Au$ heterostructure. a, Topography (grey scale images) and THz near-field images of different parts of one Ag_2Te. Images were recorded with a Au-coated Team Nanotec tip with 250 nm apex radius. In the center of the near-field image at 4.25 THz we show an in-plane wavevector diagram, where the green dots show the real part of the APP wavevector perpendicular to the edges e_1, e_2, and e_3. The black solid line represents an ellipse. **b,** Illustration of the s-SNOM experiment (analogue to Fig. 1a) with a sample comprising an h = 135 nm thick Ag_2Te platelet on top of a t = 52 nm thick SiO_2 layer on top of a 50 nm thick Au film. **c,** Line profiles across (perpendicular to) the edges e_1, e_2, and e_3 showing topography, near-field amplitude s_3 and near-field phase φ_3 at 4.25 THz. The positions of 0 nm correspond to the platelet edges. Grey and white background marks the substrate and platelet area, respectively. Black solid lines show fits to the experimental data with a radially propagating damped wave. **d,** APP dispersion perpendicular to the platelet edges e_1 (blue), e_2 (red), and e_3 (violet). Symbols represent experimental values obtained from fitting near-field amplitude and line profiles for different frequencies, as illustrated in Fig. 2c for 4.25 THz. Solid lines are linear guides to the eye.

The relative propagation length of the polaritons, L/λ_p, is rather short, challenging the measurement of the polariton wavelength λ_p and polariton dispersion. As discussed in refs.[37,38], one can increase L/λ_p by placing the layer that supports polaritons onto a thin dielectric layer on top of a metal surface (Methods), such that acoustic polaritons (also referred as to image polaritons[38,39]) are formed. The coupling of the polaritons

with their mirror image in the metal surface has the further advantages that λ_p is reduced and that an exceptional strong field concentration inside the spacer can be achieved[5,28,37,38,40]. We adopted this idea and placed a Ag_2Te platelet onto a thin SiO_2 layer on a Au layer (Fig. 2). The THz near-field images of the $Ag_2Te/SiO_2/Au$ heterostructure reveal up to three narrow polariton fringes parallel to the edges e_2 and e_3 (Fig. 2a), contrary to only one fringe observed on the platelets on Si (Fig. 1c,d). Importantly, the polariton wavelength (i.e. fringe spacing and width) still depends on the propagation direction (similar to theoretical predictions for other APPs[41,42]) and is smaller for the polaritons propagating perpendicularly to edge e_1.

For better understanding the APPs, we recorded amplitude- and phase-resolved THz near-field line profiles across the platelet edges e_1, e_2 and e_3 (marked in the 4.25 THz image shown in Fig. 2a). Complex-valued fitting of both amplitude s_3 and phase φ_3 line profiles (established in Ref.[29] and shown in Fig. 2c) with a radially propagating damped wave yields the complex-valued polariton wavevectors $k_{p.i}$ perpendicular to the edges e_i (Methods and Supplementary Note S3). The real part of the wavevectors, $k'_{p,i}$ (green dots), is shown in the wavevector diagram plotted in the center of the near-field image at 4.25 THz (Fig. 2a), indicating an elliptical isofrequency contour (solid line), which could origin from an in-plane anisotropic effective electron mass in Ag_2Te, an in-plane anisotropic high-frequency permittivity, or both (see further discussion below).

To determine the polariton dispersion, $\omega(k'_{p,i})$, we recorded amplitude- and phase-resolved THz near-field line profiles across the platelet edges e_1, e_2 and e_3 at various frequencies f and fitted them analogue to Fig. 2c. We find a nearly linear polariton dispersion for the lower frequencies (Fig. 2d), which is a typical characteristic of acoustic modes. From the slopes we find large PP wavelength compressions (relative to the photon wavelength λ_0) of about $\lambda_{p,1}/\lambda_0 \sim 1/42$, $\lambda_{p,2}/\lambda_0 \sim 1/27$, and $\lambda_{p,3}/\lambda_0 \sim 1/27$, respectively, providing first experimental evidence of ultra-confined anisotropic APPs.

Surprisingly, the elliptical isofrequency curve indicates a rather high-symmetry APP propagation, which cannot be straightforwardly connected to the non-orthogonal

platelet edges and the low-symmetry monoclinic crystal structure of Ag_2Te. Indeed, a recent study of PhPs on monoclinic β-phase Ga_2O_3 (bGO) reports the emergence of shear polaritons featuring tilted wavefronts and asymmetric polariton responses[7,8], which we did not observe in Fig. 1 and 2. We clarify this observation in the following by establishing a geometric connection between the APP propagation and the crystal structure of Ag_2Te.

We first verified the elliptical isofrequency curve and its main axes. To that end, we fabricated (Supplementary Note S4) a disk (Fig. 3b) from one $Ag_2Te/SiO_2/Au$ heterostructure (Fig. 3a), such that all APP directions can be probed. The THz near-field image at 4.25 THz (Fig. 3d) reveals more than two interference fringes all around the disk circumference. Their spacing has a minimum in *x*-direction (perpendicular to edge e_1) and increases continuously to reach its maximum in *y*-direction (which is non-orthogonal to any of the platelet edges). Fourier transform (FT) of the image (Supplementary Note S5) confirms the elliptical isofrequency contour (Fig. 2a). In contrast to Fig. 2, we now see more than two interference fringes in all propagation directions and that the fringe spacing is reduced. This further compression of the polariton wavelength (up to $\lambda_p/\lambda_0 = 1/65$) was achieved by reducing the thickness of the SiO_2 spacer from 52 nm to 17 nm, i.e., by increasing the coupling between platelet PPs and their image in the Au surface.

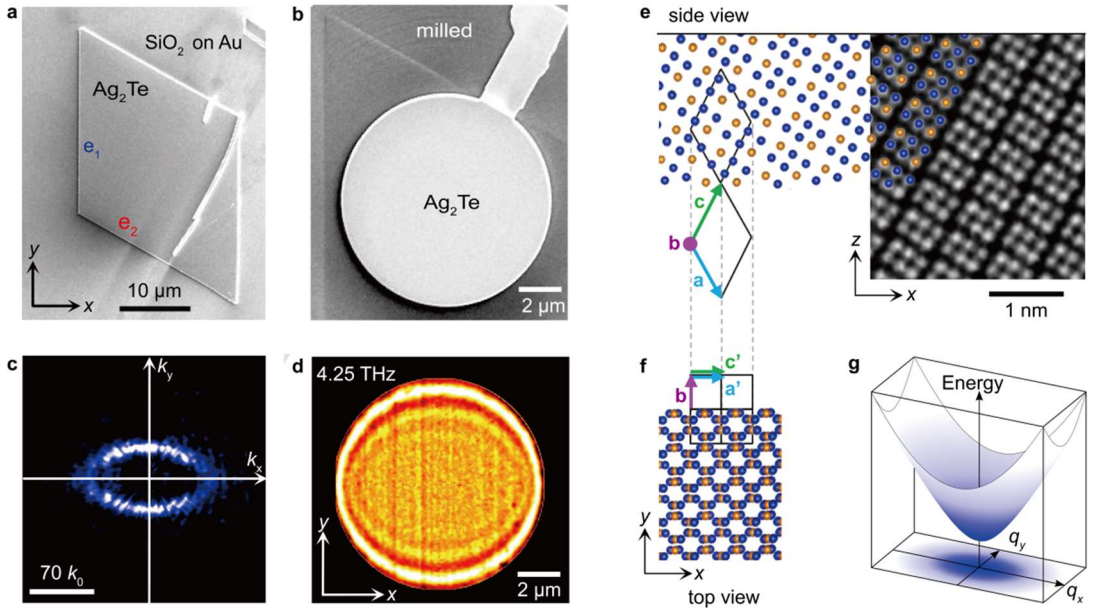

Fig. 3 | Relationship between anisotropic APP propagation, platelet geometry and crystal lattice structure. a, Scanning electron microscopy (SEM) image of a 135 nm thick Ag_2Te platelet on top of a 17 nm thick SiO_2 layer on top of an Au layer. **b,** SEM image of a Ag_2Te disk, which was obtained by focused ion beam (FIB) milling of the Ag_2Te platelet shown in panel a. **c,** FT of the THz near-field images shown in panel d. **d,** Near-field image of the Ag_2Te disk shown in panel b, recorded at 4.25 THz. Image processing (described in Supplementary Note S5) was applied for better visibility of the polariton fringes. **e,** STEM (grey scale) image of a cross-section of a Ag_2Te platelet. The cross-section is oriented perpendicular to the Ag_2Te platelet´s monoclinic unit cell axis **b**, which is parallel to the platelet surface. The blue and orange dots represent the Ag and Te atoms of the monoclinic Ag_2Te (Hessite) crystal structure (ID: mp-1592; space group: $P2_1/c$ (No. 14); Point group: C_{2h} (2/m); DOI: 10.17188/1191458) and were matched to the STEM image. The arrows labeled **a**, **b** and **c** represent the unit cell vectors. **f,** Top view of the crystal structure. The arrows labeled **a**´ and **c**´ represent the projection of the corresponding unit cell vectors onto the *x*-*y* plane (surface plane). **g,** Band structure of Ag_2Te in the *x*-*y* plane, showing the electron energy as a function of the electron momenta in *x*- and *y*-direction, q_x and q_y.

To understand the relationship between the main axes of the elliptical isofrequency contour and the crystal structure of the Ag_2Te platelets, we took a STEM image of a platelet cross-section (grey-scale image in Fig. 3e,f) that is oriented perpendicular to the platelet edge e_1 (Supplementary Note S6). The arrangement of atoms (white dots) can be well matched by the crystal structure of monoclinic Ag_2Te (blue and orange dots represent Ag and Te atoms) when the unit cell vector **b** (the one being orthogonal to both the **a** and **c** axes) is oriented parallel to the platelet surface and edge e_1. The vector **b** is thus orthogonal to the projections of the unit cell vectors **a** and **c** onto the platelet surface, **a**´ and **c**´, which explains the high-symmetry elliptical isofrequency contour of

Fig. 3c and its orientation, and thus the high-symmetry yet anisotropic PP propagation. For other crystal orientations, for which the projections of the unit cell vectors onto the platelet surface were non-orthogonal, shear polaritons may be observed[7,8].

Based on the Ag_2Te crystal structure and its orientation, we performed first-principles calculations of the two-dimensional electronic band structure parallel to the platelet surface (Fig. 3g and Supplementary Note S7). The band structure can be well approximated by an elliptical paraboloid with the minimum at the Γ-point, which allows for describing the electronic properties and dielectric function of the Ag_2Te platelets by an anisotropic Drude model. For a quantitative analysis of the experimental polariton dispersions and isofrequency contours we thus model the Ag_2Te platelet as a layer of zero thickness[43,44] that is characterized by an anisotropic sheet (2D) conductivity

$$\hat{\sigma}(\omega) = \mathrm{i}\omega\varepsilon_0 h(\hat{\mathrm{I}} - \hat{\varepsilon}(\omega)), \qquad (1)$$

where $\hat{\varepsilon}(\omega)$ is a 2x2 anisotropic permittivity tensor describing the surface plane of the Ag_2Te platelet, $\hat{\mathrm{I}}$ the identity tensor, ε_0 is the vacuum permittivity and $\omega = 2\pi f$. Since the projection of the unit cell onto the platelet surface is orthogonal (Fig. 3e), the tensors $\hat{\varepsilon}(\omega)$ and $\hat{\sigma}(\omega)$ are diagonal in the *x*-*y* coordinate system defined in Fig. 3a. According to the Drude model, the diagonal permittivity tensor elements can be described as

$$\varepsilon_{xx}(\omega) = \varepsilon_{\mathrm{IR},x} - \frac{\omega_{\mathrm{p},x}^2}{\omega^2 + \mathrm{i}\gamma_x\omega} \quad \text{and} \quad \varepsilon_{yy}(\omega) = \varepsilon_{\mathrm{IR},y} - \frac{\omega_{\mathrm{p},y}^2}{\omega^2 + \mathrm{i}\gamma_y\omega}, \qquad (2)$$

where $\varepsilon_{\mathrm{IR},i}$ (i = *x*,*y*) are the directional high-frequency (infrared) permittivities of Ag_2Te, γ_i the directional charge carrier damping (inverse of the carrier scattering time), and

$$\omega_{\mathrm{p},i} = 2\pi f_{\mathrm{p},i} = \left(ne^2/\left(m_{\mathrm{eff},i}\varepsilon_0\right)\right)^{1/2} \qquad (3)$$

the (unscreened) directional plasma frequencies with $m_{\mathrm{eff},i}$ being the directional effective carrier masses, n the carrier concentration and e the electron charge. Considering further that the conductivity sheet is located on a thin dielectric spacer on

a perfect metal conductor (representing the Au surface), we obtain an analytical description of the dispersion relation of the in-plane anisotropic APPs (Supplementary Note S8), which we can use to fit simultaneously the experimentally measured polariton dispersions $\omega(k_{p,i})$ using $\omega_{\mathrm{p},i}$, γ_i and $\varepsilon_{\mathrm{IR},x}$ as fit parameters and setting $\varepsilon_{\mathrm{IR},y} \approx 1.9\varepsilon_{\mathrm{IR},x}$ and $(\varepsilon_{\mathrm{IR},x}+\varepsilon_{\mathrm{IR},y})/2 = 11$ (derived from s-SNOM imaging of Ag_2Te platelets at mid-infrared frequencies described in Supplementary Note S9 to S11).

We apply the theoretical description above to analyze in Fig. 4 the experimental polariton data shown in Fig. 2d. In Fig. 4a we show the whole Ag_2Te platelet and indicate by the dashed lines where THz near-field amplitude and line profiles were measured, yielding the APP dispersions shown in Fig. 4b (symbols, same data as in Fig. 2d). We achieved an excellent fitting of the polariton dispersions (solid lines in Fig. 4b) for $f_{\mathrm{p},x}$= 28.9 THz, $f_{\mathrm{p},y}$= 44.3 THz, γ_x = 2.4 THz and γ_y = 0.9 THz, confirming the nearly linear dispersion that is characteristic for APPs. We use the fit parameters to calculate (Supplementary Note 8) and theoretically compare the electric field (vertical component Re(E_z)) distribution and isofrequency curves of the APPs (Fig. 4c,d) and PPs in Ag_2Te platelets on a semi-infinite SiO_2 substrate (Fig. 4e,f). We obtain elliptical isofrequency contours for both APPs and PPs, which confirms that that the propagation anisotropy is qualitatively preserved after the hybridization of PPs with their mirror image in the Au substrate (Fig. 4c,d). The calculated field profiles further confirm the increased relative propagation length of the APPs, and that their wavevectors and field confinement are significantly enhanced compared to that of the PPs, i.e. that the APP wavelength and field decay in the vertical (z-) direction is strongly reduced (Fig. 4c,e). A zoom into the field distribution of the APPs (right side of Fig. 4c) also confirms the highly concentrated electric field inside the SiO_2 spacer, which is formed by the charges in the Ag_2Te platelet and their mirror image in the Au surface. We note that our theory can be also applied when the 2D conductivity tensor of a thin layer above a metal surface is non-diagonal. In this case, we expect acoustic shear polaritons, where both the in-plane anisotropy and shearing properties are qualitatively retained.

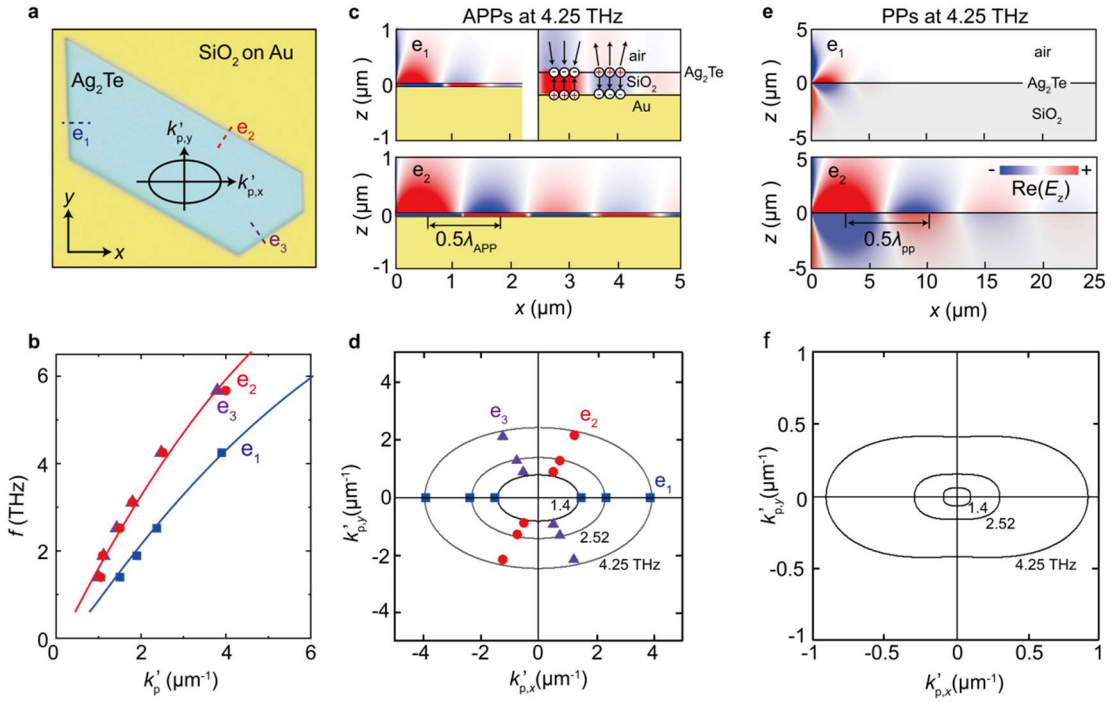

Fig. 4 | PP dispersions and isofrequency curves. a, Light microscope image of the Ag_2Te platelet on a SiO_2 thin layer on Au, which is discussed in Fig. 2. The diagram shows the isofrequency contour of the APPs. **b,** APP dispersion perpendicular to the platelet edges e_1 (blue), e_2 (red) and e_3 (violet), as obtained from near-field line profiles recorded along the dashed lines in panel **a**. Symbols show the experimental data of Fig. 2d. Solid lines show the fits described in the text. **c,** Calculated near-field distribution (real part of the vertical electric field, Re(E_z)) of APPs at 4.25 THz, which propagate radially and perpendicular to the platelet edges e_1 and e_2 (upper and lower panel, respectively). The 135 nm thick platelet on a 52 nm thick SiO_2 layer on Au is described as a 2D sheet with a conductivity obtained from the fit of the APP dispersion of panel **b**. The right side shows a zoom into the spacer region, illustrating the charges in the Ag_2Te sheet, the image charges in the Au surface and the associated electric field distribution. **d,** Solid lines show the calculated isofrequency contours of APPs. The material parameters are the same as in panel **c**. The symbols show the experimental data of panel **b**. **e,** Calculated near-field distribution (real part of the vertical electric field, Re(E_z)) of radially propagating PPs at 4.25 THz, which propagate perpendicular to the platelet edges e_1 and e_2 (upper and lower panel, respectively). The 135 nm thick platelet on top of SiO_2 is described and shown as a 2D sheet with a conductivity obtained from the fit of the PP dispersion of panel b. **f,** Calculated isofrequency contours of PPs. The material parameters are the same as in panel e.

APP interferometry can be applied to measure optically and at room temperature the anisotropic effective carrier mass. We find $m_{\mathrm{eff},x}/m_{\mathrm{eff},y} = f_{\mathrm{p},y}^2/f_{\mathrm{p},x}^2 \approx 2.4$, which we attribute to the in-plane anisotropic band structure of the Ag_2Te platelets[33,45,46]. To obtain the effective carrier masses we performed Hall measurements of the carrier concentration in one of the Ag_2Te platelets, yielding $n \approx 1.65 \cdot 10^{18}$ cm^{-3}

(Supplementary Note 12). Using Eq. (3), we obtain $m_{\mathrm{eff},x} \approx 0.16 m_{\mathrm{e}}$ and $m_{\mathrm{eff},y} \approx 0.07 m_{\mathrm{e}}$, where m_{e} is the electron mass, matching well the values from literature[33,35,47] and our band structure calculations, $m_{\mathrm{eff},x} \approx 0.18 m_{\mathrm{e}}$ and $m_{\mathrm{eff},y} \approx 0.06 m_{\mathrm{e}}$ (Supplementary Note 7). We note that the carrier damping is anisotropic too (γ_x = 2.4 THz and γ_y = 0.9 THz), resulting in anisotropic relative APP propagation length (well seen in Fig. 2c) and APP lifetimes of $\tau_{\mathrm{APP},x}$ = 0.14 ps and $\tau_{\mathrm{APP},y}$ = 0.31 ps. Quantitative comparison with transport measurements corroborate our results (Methods). We note that Ag_2Te is a topological insulator[33,35,47], but we could explain the THz polariton dispersion exclusively based on massive bulk carriers due to the dominance of them at room temperature[35]. In the future, low-temperature s-SNOM[48] could be employed for exploring potential topological in-plane anisotropic THz APPs.

In summary, we observed in-plane anisotropic PPs in the monoclinic semiconductor Ag_2Te by real-space THz nanoimaging. We found that their confinement and relative propagation length can be increased through the fabrication of Ag_2Te/spacer/metal heterostructures, whereas the in-plane anisotropic propagation characteristic remains. These in-plane anisotropic APPs manifest multiple spatial signal oscillations even for polariton lifetimes as short as about 0.2 ps, which – from a general perspective - is critically important for exploiting in-plane anisotropic PPs for future on-chip circuitry applications or for room temperature measurements of in-plane materials properties such as directional effective charge carrier masses and charge carrier damping. The strong field concentration of APPs, particularly in the gap between the polaritonic layer and the metal surface, may be exploited for field-enhanced molecular sensing or for boosting (ultra)strong THz light-matter coupling with molecules[49], classical two dimensional electron gases[50] or quantum materials.

Methods

Growth of Ag_2Te platelets and transfer onto different substrates

High-quality Ag_2Te platelets were grown by chemical vapor deposition (CVD) using polycrystalline powder as the precursor and argon as carrier gas[35]. The furnace was heated up rapidly to the growth temperature (in the range of 950 - 1050 °C) within 20 min, held constant for 60 min, and then cooled naturally with the flow of argon. The precursor was placed in the hot center of the furnace, and c-cut sapphire substrates were put downstream.

The CVD-grown Ag_2Te platelets were transferred onto various substrates (Si, SiO_2 layer on Si, and thin SiO_2 layer on 50 nm Au layer on Si) using the polydimethylsiloxane (PDMS)-based dry-transfer method[51]. For the four-terminal electrical transport measurements, we used commercial silicon substrates covered with a 285 nm thick SiO_2 layer (Bonda Technology Pte Ltd). The SiO_2 layer on Au on Si substrates was fabricated as follows. First, a Cr layer of about 5 nm thickness was deposited by magnetron sputtering as an adhesion layer onto a Si substrate, subsequently, a 50 nm thick Au layer was sputtered onto the Cr layer. Finally, SiO_2 was sputtered onto the Au layer.

THz near-field microscopy setup

We used a THz scattering-type scanning near-field optical microscope (s-SNOM), which is based on a commercial setup from Neaspec (Germany), where a metalized atomic force microscope (AFM) tip acts as a THz near-field probe (Supplementary Figure S1). The tip is illuminated with monochromatic THz radiation from a gas laser (SIFIR-50, Coherent Inc., USA), which is focused with a parabolic mirror. Via the lightning rod effect, the tip concentrates the THz radiation into a nanoscale near-field spot at the tip apex. The tip-scattered field is recorded as a function of tip position. Collection and detection of the tip-scattered field are done with the same parabolic mirror and a cryogen-free THz Bolometer System (QMC Instruments Ltd.). To obtain background-free near-field signals, the tip is oscillated at the cantilever's mechanical resonance frequency Ω (tapping mode) and the bolometer signal is demodulated at the

third harmonic of the oscillation frequency, 3Ω. To increase the signal-to-noise ratio, we used commercial gold tips with a large apex radius of about 250 nm (Team Nanotec LRCH). They were oscillated at a frequency of about $\Omega \approx 70$ kHz with an amplitude of about 150 nm.

The near-field images shown in Fig. 1c,d, Fig. 2a and Fig. 3d were obtained by recording the tip-scattered field with a Michelson interferometer, where the reference mirror was fixed at a position where the near-field signal on the Ag_2Te platelet was maximum.

The near-field amplitude and phase line profiles in Fig. 2c and Supplementary Figure 3, s_3 and φ_3, were obtained by synthetic optical holography (SOH) [29,52-54], which is based on a Michelson interferometer where the reference mirror (mounted on a delay stage) is translated at a constant velocity along the reference beam path. The interferometric detection is key to enable a complex-valued analysis of near-field profiles, which is critical for a reliable measurement of the wavelength of polaritons with short propagation lengths.

Four-terminal electrical transport measurements

To measure the directional in-plane conductivity of a Ag_2Te platelet (Fig. 1e), we first fabricated a circle-shaped nanoplatelet with contact pads via electron beam (e-beam) lithography and ion beam etching (IBE) with argon for 3-5 minutes. The electrodes were fabricated by e-beam lithography, magnetron sputtering of Cr and Au (5 and 100 nm thickness, respectively) and lift-off. We then performed four-terminal electric transport measurement[55], which allows to eliminate the contact resistance of the interface between the gold layer and nanoplate surface (Supplementary Figure S2).

To that end, we generated an electrical current (marked by a white arrow labeled I_i in Supplementary Figure S2) through two diametrically opposed contact pads (labeled C_{I1} and C_{I2} in Supplementary Figure S2) and measured the voltage V_{ii} between the two adjacent contact pads C_{V1} and C_{V2}. The index i stands for the direction defined by the

diametrically opposed contact pads through which the current I_i flows. We obtained the resistance $R_{ii} = V_{ii}/I_i$, yielding the conductivity $\sigma_i = (R_{ii}\, hw/l)^{-1}$, where h and w are the thickness and the diameter of the Ag_2Te disk, respectively. l is the distance between C_{V1} and C_{V2}. Using $w/l = \sqrt{2}$ and h = 100 nm for Ag_2Te disk, we obtained the in-plane directional conductivity in Fig. 1e.

The brown solid curve in Fig. 1e shows a fit by $\sigma_{\max}\cos^2(\theta - \Phi) + \sigma_{\min}\sin^2(\theta - \Phi)$[56], where $\sigma_{\max}$ and $\sigma_{\min}$ are the maximum and minimum values of the sample conductivity, θ presents the directional angle where the sample conductivity is measured and Φ is the angle relative to the reference angle (here the horizontal direction).

Relative propagation length and lifetime of polaritons

The relative propagation length of the polaritons is defined as $L/\lambda_{\mathrm{p}} = k_{\mathrm{p}}' v_g \tau/(2\pi)$, where $L = 1/k_{\mathrm{p}}''$ is the polariton propagation length, $v_g = d\omega/dk_{\mathrm{p}}'$ the group velocity and k_p'' the imaginary part of the complex-valued polariton wavevector $k_{\mathrm{p}} = k_{\mathrm{p}}' + ik_{\mathrm{p}}''$. We thus find that $L/\lambda_{\mathrm{p}} \propto k_{\mathrm{p}}' v_{\mathrm{g}}$, where $v_g = d\omega/dk_{\mathrm{p}}'$ is the group velocity, showing that L/λ_{p} can be increased by increasing k_{p}' but maintaining a large v_{g}. Because of the linear dispersion of acoustic modes, the increase of k_{p}' comes along with a much smaller reduction of v_{g} as compared to increasing k_{p}' of non-acoustic polaritons. Consequently, L/λ_{p} is increased by turning polaritons in a thin layer into acoustic polaritons by placing the layer on top of a dielectric spacer on top of a metal surface.

The lifetime of polaritons can be calculated according to $\tau = L/v_g$ once their propagation length L and dispersion $\omega(k_p)$ is known. We obtained both of them by fitting the THz near-field line profiles to determine $k_{\mathrm{p}} = k_{\mathrm{p}}' + ik_{\mathrm{p}}''$, as described below.

Measurement of complex-valued polariton wavevectors

To measure the complex-valued polariton wavevector $k_{\mathrm{p},i} = k_{\mathrm{p},i}^{'} + \mathrm{i}k_{\mathrm{p},i}^{''}$, where the index *i* indicates the propagation direction, we recorded THz near-field amplitude and phase line profiles, $s_3(\xi)$ and $\varphi_3(\xi)$, across the edges e_1, e_2 and e_3 of the Ag_2Te platelet shown in Fig. 2a. ξ is the position relative to the edge of the Ag_2Te platelet. Each panel in Supplementary Figure 3 shows the topography line profile (top left diagram) and near-field amplitude and phase line profiles (symbols in middle and bottom left diagrams) across one edge at one THz frequency. The near-field amplitude and phase line profiles were normalized to the complex-valued signal *C* that is measured far away from the edge.

We obtained $k_{\mathrm{p},i}$ by complex-valued fitting of the near-field line profiles, as established in ref.[29]. To that end, we constructed complex-valued line profiles, $\sigma_3(\xi) = s_3(\xi)e^{\mathrm{i}\varphi_3(\xi)}$, and fitted them by

$$E_{\mathrm{p}} = A\mathrm{e}^{\mathrm{i}2k_{\mathrm{p},i}\xi}/\sqrt{2\xi} + C, \qquad (4)$$

which describes the electric field of a back-reflected, radially (i.e. tip-launched) propagating damped wave (black curves in Supplementary Figure S3). The fitting parameters are *A*, $k_{\mathrm{p},i}$ and *C*. The real part of $k_{\mathrm{p},i}$ is shown by the symbols in Fig. 2d and Fig. 4b.

Preparation of sample cross-section and STEM analysis

The STEM image shown in Fig. 3e was obtained from a TEM lamella prepared by a standard FIB lift-out technique (using a Helios 600 Nanolab Dual Beam system) from the Ag_2Te platelet shown in Supplementary Figure S6. The orientation of the lamella (marked by the red line) is perpendicular to the platelet surface and parallel to the *x* axis (perpendicular to the edge e_1) as defined in Fig. 3. It was determined from an s-SNOM image recorded at 4.25 THz (color scale image in Supplementary Figure S6), where we can clearly identify the edge e_1, where polariton fringes are more closely spaced.

STEM imaging has been performed on a Titan 60-300 (S)TEM equipped with x-FEG and a retractable HAADF STEM detector at 300 kV accelerating voltage. The optimal beam convergence semi-angle for these conditions was 10 mrad.

Comparison of anisotropic carrier properties from polariton interferometry and electrical transport measurements

To corroborate the anisotropic carrier properties, we use the effective carrier masses and carrier damping to calculate the DC conductivity according to $\sigma_{\mathrm{DC,i}} = ne^2/(\gamma_\mathrm{i} m_{\mathrm{eff,i}})$. We obtain $\sigma_{\mathrm{DC,x}} \approx 1.3{\cdot}10^5$ S/m and $\sigma_{\mathrm{DC,y}} \approx 5.7{\cdot}10^5$ S/m, which differ by only a factor of two from the transport measurements shown in Fig. 1e. We attribute this discrepancy to different charge carrier concentrations *n* in the different Ag_2Te platelets that were used for the electrical transport measurements and polariton interferometry. On the other hand, most importantly, the ratio between the conductivities in the *y*- and *x*-direction – which is a consequence of the anisotropy of effective mass and damping – is nearly the same in the transport ($\sigma_{\mathrm{DC,x}}/\sigma_{\mathrm{DC,y}} \approx \sigma_{\mathrm{DC,x}}/\sigma_{\mathrm{DC,y}} = 0.75{\cdot}10^5/\ 3.08{\cdot}10^5 \approx 0.24$) and polariton interferometry ($\sigma_{\mathrm{DC,x}}/\sigma_{\mathrm{DC,y}} \approx 0.21$) measurements.

Acknowledgements

This work was supported by the Spanish Ministry of Science and Innovation under the María de Maeztu Units of Excellence Program (CEX2020-001038-M) and the Projects RTI2018-094861-B-100 and PID2021-123949OB-I00. F. X. Xiu acknowledges the financial support from the National Natural Science Foundation of China (52225207, 52150103 and11934005) and the Shanghai Pilot Program for Basic Research - Fudan University 21TQ1400100(21TQ006). I.N. acknowledges financial support from the German Research Foundation (DFG) under project no. 467576442. B.M-G. thanks Gipuzkoa Council (Spain) in the frame of Gipuzkoa Fellows Program. M.G.V., I. E. and M.G.A acknowledge the Spanish Ministerio de Ciencia e Innovacion (grant PID2019- 109905GB-C21). M.G.V. is also thankful to the Deutsche Forschungsgemeinschaft (DFG, German Research Foundation) GA 3314/1-1 – FOR 5249 (QUAST). A.K. acknowledges the support of the Czech Science Foundation

GACR under the Junior Star grant No. 23-05119M. S.C acknowledges the support of the National Natural Science Foundation of China (NSFC, Grants No. 61988102) and the support of Science and Technology Commission of Shanghai Municipality (No. 23010503400).

Corresponding authors

Correspondence to Rainer Hillenbrand and Faxian Xiu.

Competing interests

R.H. is co-founder of Neaspec GmbH, a company producing scattering-type scanning near-field optical microscope systems, such as the one used in this study. The remaining authors declare no competing interests.

References

1 Basov, D. N., Asenjo-Garcia, A., Schuck, P. J., Zhu, X. & Rubio, A. Polariton panorama. *Nanophotonics* **10**, 549-577 (2020).

2 Daniel Rodrigo *et al.* Mid-infrared plasmonic biosensing with graphene. *Science* **349**, 165-168 (2015).

3 Basov, D. N., Fogler, M. M. & Garcia de Abajo, F. J. Polaritons in van der Waals materials. *Science* **354**, aag1992-1991-1998 (2016).

4 Tielrooij, K. J. *et al.* Out-of-plane heat transfer in van der Waals stacks through electron-hyperbolic phonon coupling. *Nat. Nanotechnol* **13**, 41-46 (2018).

5 Lee, I. H., Yoo, D., Avouris, P., Low, T. & Oh, S. H. Graphene acoustic plasmon resonator for ultrasensitive infrared spectroscopy. *Nat. Nanotechnol* **14**, 313-319 (2019).

6 Bylinkin, A. *et al.* Real-space observation of vibrational strong coupling between propagating phonon polaritons and organic molecules. *Nature Photon.* **15**, 197-202 (2020).

7 Passler, N. C. *et al.* Hyperbolic shear polaritons in low-symmetry crystals. *Nature* **602**, 595-600 (2022).

8 Hu, G. *et al.* Real-space nanoimaging of hyperbolic shear polaritons in a monoclinic crystal. *Nat Nanotechnol* **18**, 64-70 (2023).

9 Dai, S. *et al.* Tunable phonon polaritons in atomically thin van der Waals crystals of boron nitride. *Science* **343**, 1125-1129 (2014).

10 Caldwell, J. D. *et al.* Sub-diffractional volume-confined polaritons in the natural hyperbolic material hexagonal boron nitride. *Nat. Commun.* **5**, 5221 (2014).

11 Yoxall, E. *et al.* Direct observation of ultraslow hyperbolic polariton propagation with negative phase velocity. *Nature Photon.* **9**, 674-678 (2015).

12 Zheng, Z. *et al.* Highly confined and tunable hyperbolic phonon polaritons in van der Waals semiconducting transition metal oxides. *Adv. Mater* **30**, e1705318 (2018).

13 Ma, W. *et al.* In-plane anisotropic and ultra-low-loss polaritons in a natural van der Waals crystal. *Nature* **562**, 557-562 (2018).

14 Zheng, Z. *et al.* A mid-infrared biaxial hyperbolic van der Waals crystal. *Sci. Adv* **5**, eaav8690 (2019).

15 Caldwell, J. D. *et al.* Photonics with hexagonal boron nitride. *Nat. Rev. Mater.* **4**, 552-567 (2019).

16 Taboada-Gutierrez, J. *et al.* Broad spectral tuning of ultra-low-loss polaritons in a van der Waals crystal by intercalation. *Nat. Mater.* **19**, 964-968 (2020).

17 Ma, W. *et al.* Ghost hyperbolic surface polaritons in bulk anisotropic crystals. *Nature* **596**, 362-366 (2021).

18 Zhang, Q. *et al.* Interface nano-optics with van der Waals polaritons. *Nature* **597**, 187-195 (2021).

19 Wu, Y. *et al.* Manipulating polaritons at the extreme scale in van der Waals materials. *Nat. Rev. Phys.*, doi:10.1038/s42254-022-00472-0 (2022).

20 Low, T. *et al.* Polaritons in layered two-dimensional materials. *Nat Mater* **16**, 182-194 (2017).

21 Low, T. *et al.* Plasmons and screening in monolayer and multilayer black phosphorus. *Phys. Rev. Lett.* **113**, 106802 (2014).

22 Lian, C. *et al.* Integrated Plasmonics: Broadband Dirac Plasmons in Borophene. *Phys. Rev. Lett.* **125**, 116802 (2020).

23 Torbatian, Z., Novko, D. & Asgari, R. Hyperbolic plasmon modes in tilted Dirac cone phases of borophene. *Phys. Rev. B* **104**, 075432 (2021).

24 Huang, X. *et al.* Black phosphorus carbide as a tunable anisotropic plasmonic metasurface. *ACS Photonics* **5**, 3116-3123 (2018).

25 Wang, C. *et al.* Van der Waals thin films of WTe_2 for natural hyperbolic plasmonic surfaces. *Nat. Commun.* **11**, 1158 (2020).

26 Chen, J. N. *et al.* Optical nano-imaging of gate-tuneable graphene plasmons. *Nature* **487**, 77-81 (2012).

27 Fei, Z. *et al.* Gate-tuning of graphene plasmons revealed by infrared nano-imaging. *Nature* **487**, 82-85 (2012).

28 Alonso-Gonzalez, P. *et al.* Acoustic terahertz graphene plasmons revealed by photocurrent nanoscopy. *Nat. Nanotechnol.* **12**, 31-35 (2017).

29 Chen, S. *et al.* Real-space nanoimaging of THz polaritons in the topological insulator Bi_2Se_3. *Nat. Commun.* **13**, 1374 (2022).

30 Ju, L. *et al.* Graphene plasmonics for tunable terahertz metamaterials. *Nat. Nanotechnol.* **6**, 630 (2011).

31 Soltani, A. *et al.* Direct nanoscopic observation of plasma waves in the channel of a graphene field-effect transistor. *Light. Sci. Appl.* **9**, 97 (2020).

32 Pogna, E. A. A. *et al.* Mapping propagation of collective modes in Bi_2Se_3 and $Bi_2Te_{2.2}Se_{0.8}$ topological insulators by near-field terahertz nanoscopy. *Nat. Commun.* **12**, 6672 (2021).

33 Zhang, W. *et al.* Topological aspect and quantum magnetoresistance of beta-Ag_2Te. *Phys. Rev. Lett.* **106**, 156808 (2011).

34 Yeh, T.-T. *et al.* The optical properties of Ag_2Te crystals from THz to UV. *J. Alloys Compd.* **725**, 433-440 (2017).

35 Leng, P. *et al.* Gate-tunable surface states in topological insulator beta-Ag_2Te with high mobility. *Nano. Lett.* **20**, 7004-7010 (2020).

36 Dai, S. *et al.* Phonon polaritons in monolayers of hexagonal boron nitride. *Adv. Mater.* **31**, e1806603 (2019).

37 Menabde, S. G. *et al.* Real-space imaging of acoustic plasmons in large-area graphene grown by chemical vapor deposition. *Nat. Commun.* **12**, 938 (2021).

38 Menabde, S. G., Heiden, J. T., Cox, J. D., Mortensen, N. A. & Jang, M. S. Image polaritons in van der Waals crystals. *Nanophotonics* **11**, 2433-2452 (2022).

39 Lee, I. H. *et al.* Image polaritons in boron nitride for extreme polariton confinement with low losses. *Nat. Commun.* **11**, 3649 (2020).

40 Autore, M. & Hillenbrand, R. What momentum mismatch? *Nat. Nanotechnol.* **14**, 308-309 (2019).

41 Lee, I.-H. *et al.* Anisotropic acoustic plasmons in black phosphorus. *ACS Photonics* **5**, 2208-2216 (2018).

42 Lyu, W. *et al.* Anisotropic acoustic phonon polariton-enhanced infrared spectroscopy for single molecule detection. *Nanoscale* **13**, 12720-12726 (2021).

43 Gomez-Diaz, J. S., Tymchenko, M. & Alu, A. Hyperbolic plasmons and topological transitions over uniaxial metasurfaces. *Phys. Rev. Lett.* **114**, 233901 (2015).

44 Nikitin, A. Y. *in World Scientific Handbook of Metamaterials and Plasmonics*. *Vol 4: Recent progress in the field of nanoplasmonics (ed. Aizpurua, J.) (World Scientific, 2017).*

45 Sulaev, A. *et al.* β-Ag2Te: A topological insulator with strong anisotropy. doi:arXiv:1204.3816 (2012).

46 Sulaev, A. *et al.* Experimental evidences of topological surface states of β-Ag_2Te. *AIP Advances* **3**, 032123 (2013).

47 Lee, S. *et al.* Single crystalline beta-Ag_2Te nanowire as a new topological insulator. *Nano. Lett.* **12**, 4194 (2012).

48 Ni, G. X., Mcleod, A. S., Sun, Z., Xiong, L., Post, K. W., Sunku, S. S., Jiang, B. Y., Hone, J., Dean, C. R., Folger, M. M. and Basov, D. N. Fundamental limits to graphene plasmonics. *Nature* **557**, 530-533 (2018).

49 Damari, R. *et al.* Strong coupling of collective intermolecular vibrations in organic materials at terahertz frequencies. *Nat Commun* **10**, 3248(2019).

50 Scalari, G., Maissen, C., Turcinková, D., Hagenmüller,D., De Liberato, S., Ciuti, C., Reichl, C., Schuh, D. , Wegscheider, W., Beck, M.,Faist, J. Ultrastrong coupling of the cyclotron transition of a 2D electron gas to a THz metamaterial. *Science* **335**, 1323-1326 (2012).

51 Wang, L. *et al.* One-dimensional electrical contact to a two-dimensional material. *Science* **342**, 614-617 (2013).

52 Schnell, M., Carney, P. S. & Hillenbrand, R. Synthetic optical holography for rapid nanoimaging. *Nat Commun* **5**, 3499 (2014).

53 Maissen, C., Chen, S., Nikulina, E., Govyadinov, A. & Hillenbrand, R. Probes for ultrasensitive THz nanoscopy. *ACS Photonics* **6**, 1279-1288 (2019).

54 Chen, C. *et al.* Terahertz Nanoimaging and Nanospectroscopy of Chalcogenide Phase-Change Materials. *ACS Photonics* **7**, 3499-3506(2020).

55 Lohmann, T., Klitzing, K. V. & Smet, J. H. Four-terminal magneto-transport in graphene p-n junctions created by spatially selective doping. *Nano Lett.* **9**, 1973-1979 (2009).

56 Zhong, M. *et al.* In-plane optical and electrical anisotropy of 2D black arsenic. *ACS Nano* **15**, 1701-1709 (2021).